[Journal of Geophysical Research: Solid Earth]

Supporting Information for

Sub-decadal Volcanic Tsunamis Due to Submarine Trapdoor Faulting at Sumisu Caldera in the Izu-Bonin Arc

Osamu Sandanbata[1,2†], Shingo Watada[1], Kenji Satake[1], Hiroo Kanamori[3], Luis Rivera[4], and Zhongwen Zhan[3]

[1]Earthquake Research Institute, the University of Tokyo, Bunkyo, Tokyo, Japan.

[2]National Research Institute for Earth Science and Disaster Resilience, Tsukuba, Ibaraki, Japan.

[3]Seismological Laboratory, California Institute of Technology, Pasadena, CA 91125, USA.

[4]Université de Strasbourg, CNRS, ITES UMR 7063, Strasbourg F-67084, France.

Corresponding author: Osamu Sandanbata (osm3@bosai.go.jp)

Contents of this file

Additional Supporting Information (Files uploaded separately)

Captions for Data Set S1

Introduction

Supporting information contains descriptions of procedures for the moment tensor analysis (Text S1), and source model variations when we assume low-velocity layer in the crust (Text S2) or non-uniform dip angle of the ring fault (Text S3). Supplementary figures and tables mentioned in Main Text and Supplementary Texts (Figures S1 to S20; Tables S1 to S3), and a caption for the supplementary dataset of the source models (Data set S1), are also contained.

Text S1. Moment tensor analysis

We perform the deviatoric moment tensor analysis using the W-phase of seismic waves (Kanamori and Rivera 2008; Duputel et al. 2012; Hayes, Rivera, and Kanamori 2009) for the four earthquakes in 1996, 2006, 2015, and 2018 at Sumisu caldera; we do not analyze the 1984 event, due to inaccessibility of good quality seismic data. We download broad-band seismic records of F-net and/or GSN within the epicentral distances of 30°. We use the same Green's functions of seismic waveforms, the same filter, and assume the same centroid location, as done for the computation of the long-period seismic waveforms in Main Text (see Section 4.3). We assume the zero-trace condition $M_{rr} + M_{\theta\theta} + M_{\phi\phi} = 0$. The optimum time-shift and half duration are assumed to be the same and determined by the grid-search method. In the inversion process, we remove clearly bad records yielding a single-record seismic misfit larger than 1.5 (Table S2). The estimated deviatoric moment tensors are shown in Table S3.

From the deviatoric moment tensors, we obtain the *resolvable moment tensors* $\boldsymbol{M_{res}}$, by excluding two elements $M_{r\theta}$ and $M_{r\phi}$ that are indeterminate from long-period seismic data (Sandanbata et al. 2021). $\boldsymbol{M_{res}}$ of the four earthquakes are shown in Figures 12a–d, and their seismograms are shown in Figures S16–S19. Following our previous study (Sandanbata et al. 2021), we examine the dominancy of the vertical-CLVD component (denoted by k_{CLVD}) and the null-axis direction (denoted by the best-fit double-couple orientation) of $\boldsymbol{M_{res}}$. Since the two parameters are controlled by the ring fault arc length and orientation, comparisons of those for the repeating earthquakes enable us to evaluate similarities in their ring fault geometries (See Section 6.3).

Text S2. Effect of a low-rigidity crust on our estimation of the ring fault dip angle

In the source modeling in Main Text, we estimated the ring fault dip angle as 85.0°, by utilizing the sensitivity of the long-period seismic amplitudes to the parameter, when we used the velocity model with V_p = 6.0 km/s, V_s = 3.5 km/s, respectively and ρ_0 = 2.6 x 10^3 kg/m^3 in the shallowest crust at < 15 km depth, and assumed the Lamé's constants of λ = 29.9 GPa and μ = 31.85 GPa (see Section 4.3). However, a previous study (Kodaira et al. 2007) suggested a lower-velocity layer with V_p of 1.8–5.8 km/s exists in the shallowest depth < ~5 km of the Izu-Bonin arc, including the region around Sumisu caldera. The low rigidity at the source may reduce the seismic amplitude and thereby affect our estimate of the ring fault dip angle. Here, we estimate an optimal dip angle considering this effect, by using their moment tensors computed assuming lower values for the Lamé's constants (λ = 9.97 GPa and μ = 10.6 GPa) for the long-period seismic waveform computations. Figure S20 demonstrates that the model with 77° yields the best agreement with the observed seismic amplitude. Thus, if we assume the value of λ and μ ranging from ~10 GPa to ~30 GPa in the shallowest crust, our estimation of the ring fault dip angle ranges from ~77° to ~85°.

Text S3. Source model with modification of the ring fault dip angle

For an additional analysis, we perform the same earthquake source modeling procedures (see Section 4) for a source structure containing a ring fault along the 2/3-

ring arc length with *nonuniform dip angles* that decrease from 87° on the northeastern part to 83° on the two ends (Figure S14). The source model with this structure inverted from the tsunami waveform data (Figures S14b–c) yields even better seismic waveform fit with a smaller misfit of 0.414 (Figures S15) than the best-fit source model with the uniform ring fault dip angle (seismic misfit of 0.425; Figure 8); for example, the waveform fits of the BHE channel of KZS, YMZ, and TYS, and the BHN channel of AMM are improved by the minimal parameter tuning.

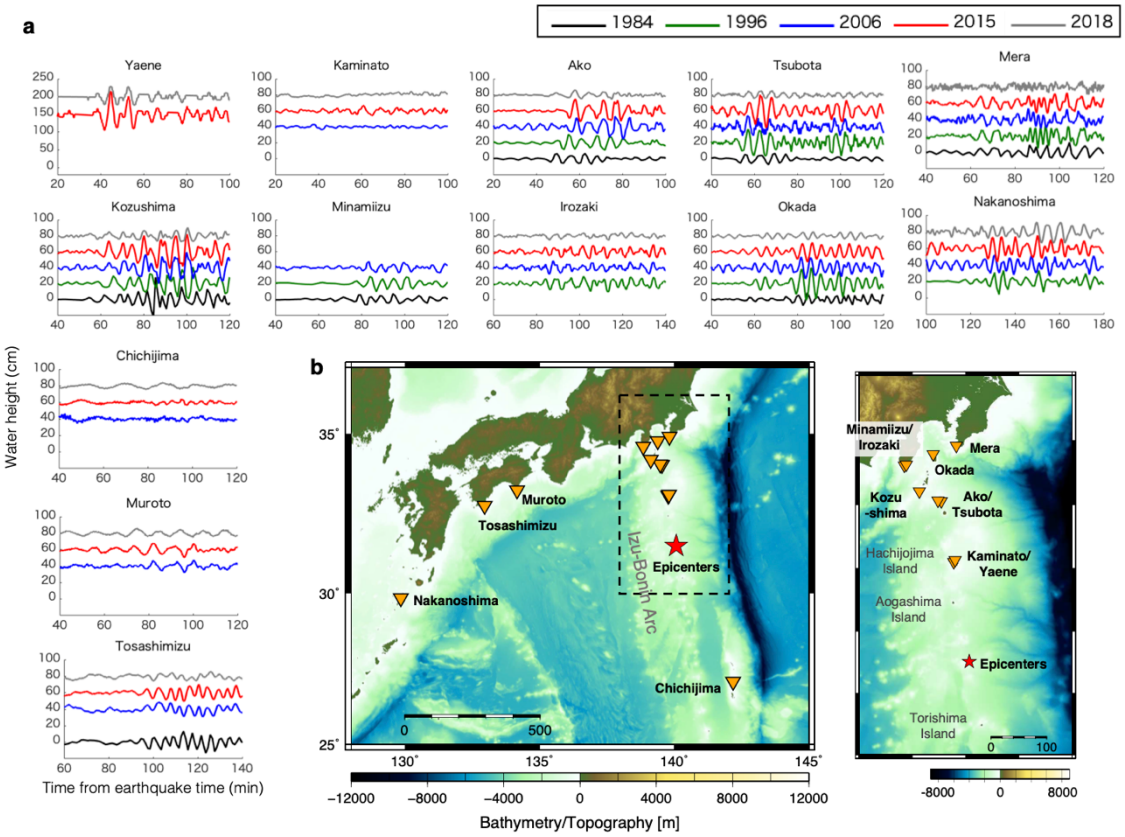

Figure S1. (**a**) Tsunami waveforms from the repeating earthquakes recorded by (**b**) tide gauge stations. In (**a**), base lines for different events are shifted by multiples of 50 cm and 20 cm in the y-axis direction for Yaene and the others, respectively. We remove the tidal trends from the raw data by the polynomial fitting. We additionally apply a band-pass filter (0.001-0.01 Hz) to the records of Tosashimizu and Chichijima to remove noise. Some records of the 1984 and 1996 events are digitized from analogue records.

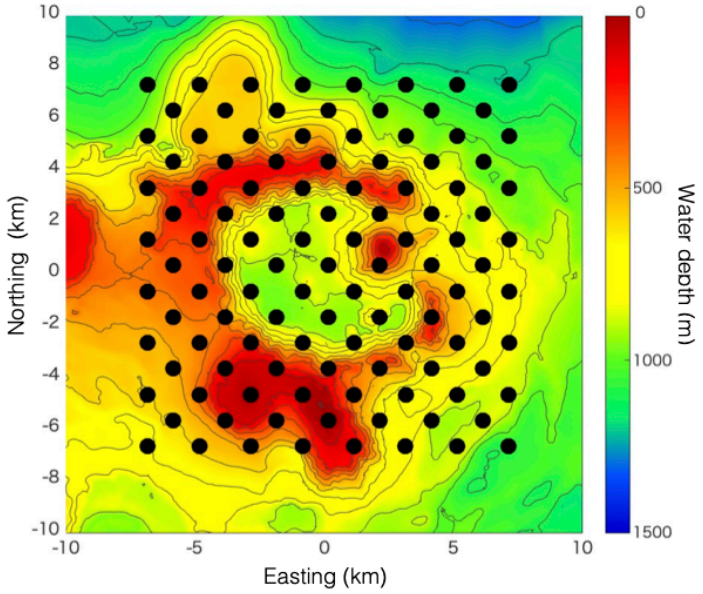

Figure S2. Unit sources of sea-surface displacement. Black dots represent central locations of 113 unit sources on the sea surface to compute the synthetic tsunami waveforms $\boldsymbol{g_j^k}$; each unit source has a cosine-tapered shape with a horizontal source size of 4 km x 4 km (Equation 1).

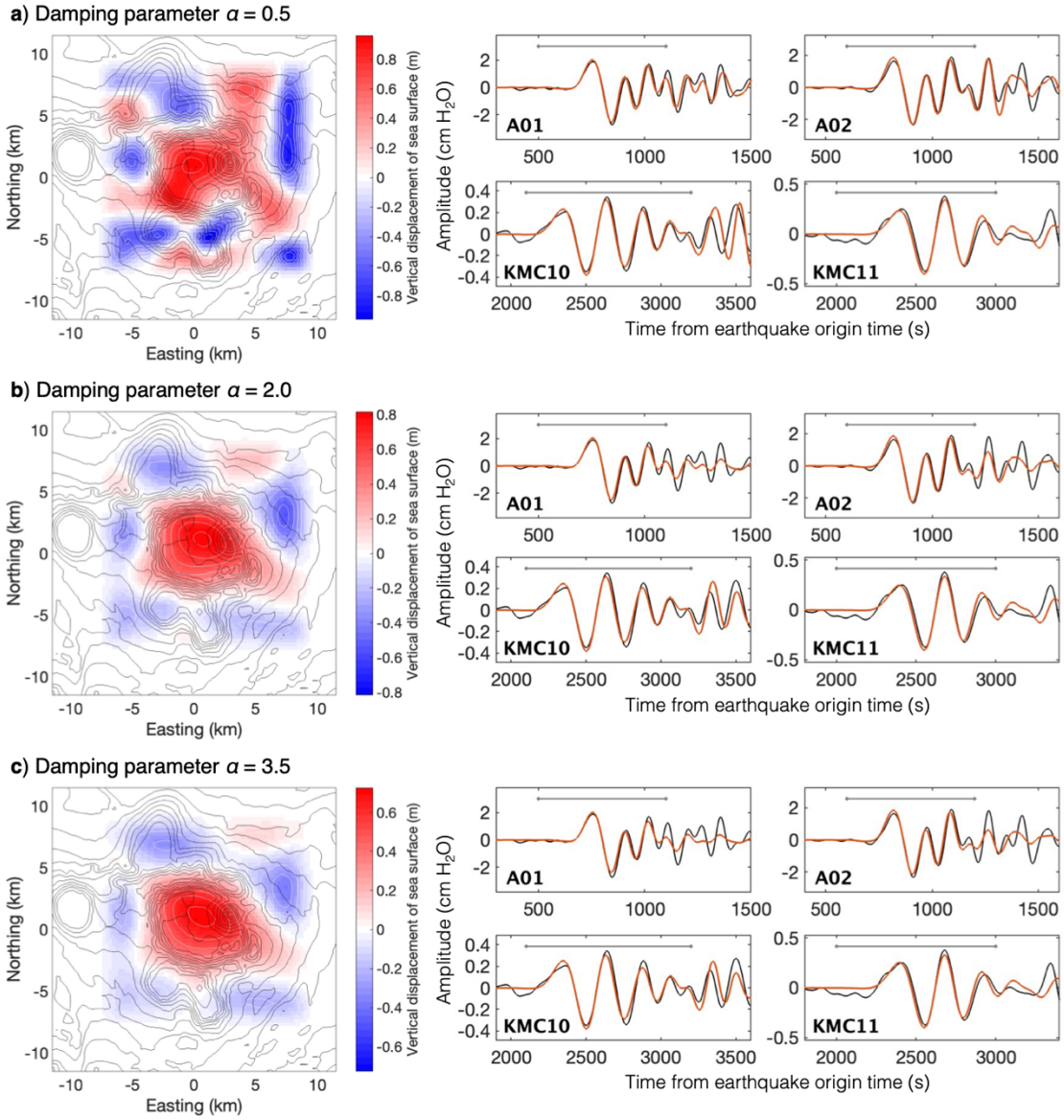

Figure S3. Results of the tsunami waveform inversion for the initial sea-surface displacement with different damping parameters α of (**a**) 0.5, (**b**) 2.0, and (**c**) 3.5 (see Section 3). By taking a balance between the waveform fit and the smoothness of the displacement, we determine α = 2.0 in this study.

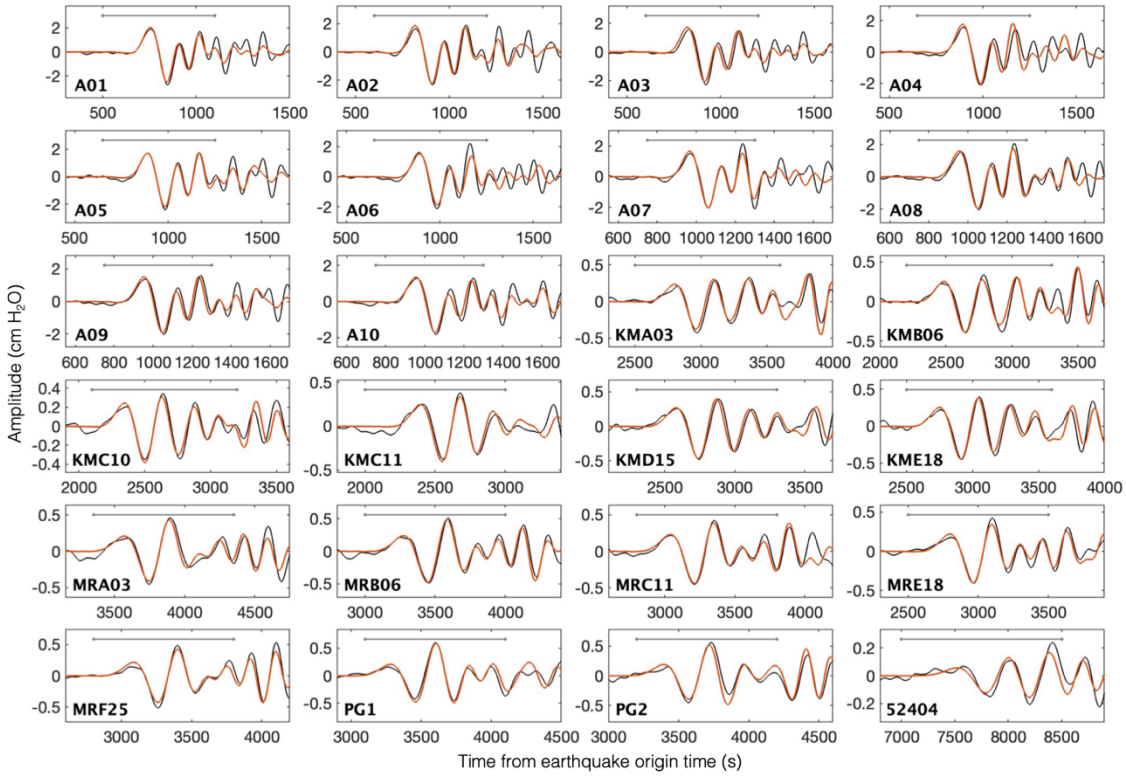

Figure S4. Comparison of the observed (black) and synthetic (red) tsunami waveforms at the ocean bottom pressure (OBP) gauges from the initial sea-surface displacement model with uplift and subsidence (Figure 2a). The gray line represents the time interval used for the inversion.

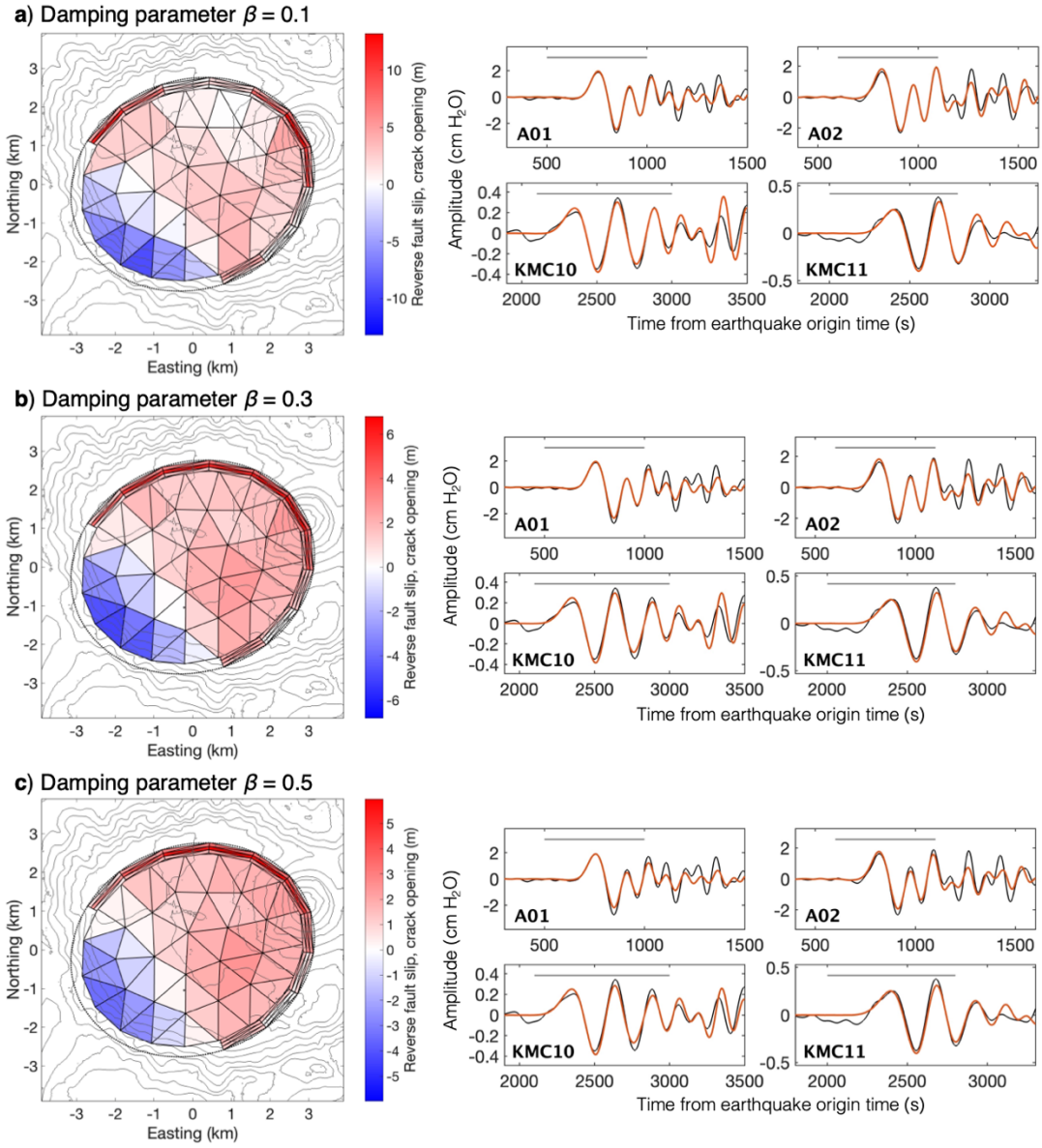

Figure S5. Results of the tsunami waveform inversion for the fault-crack composite source models with different damping parameters $\boldsymbol{\beta}$ of (**a**) 0.1, (**b**) 0.3, and (**c**) 0.5 (see Section 4.2). By taking a balance between the waveform fit and the smoothness of the motion, we determine $\boldsymbol{\beta}$ = 0.3 in this study.

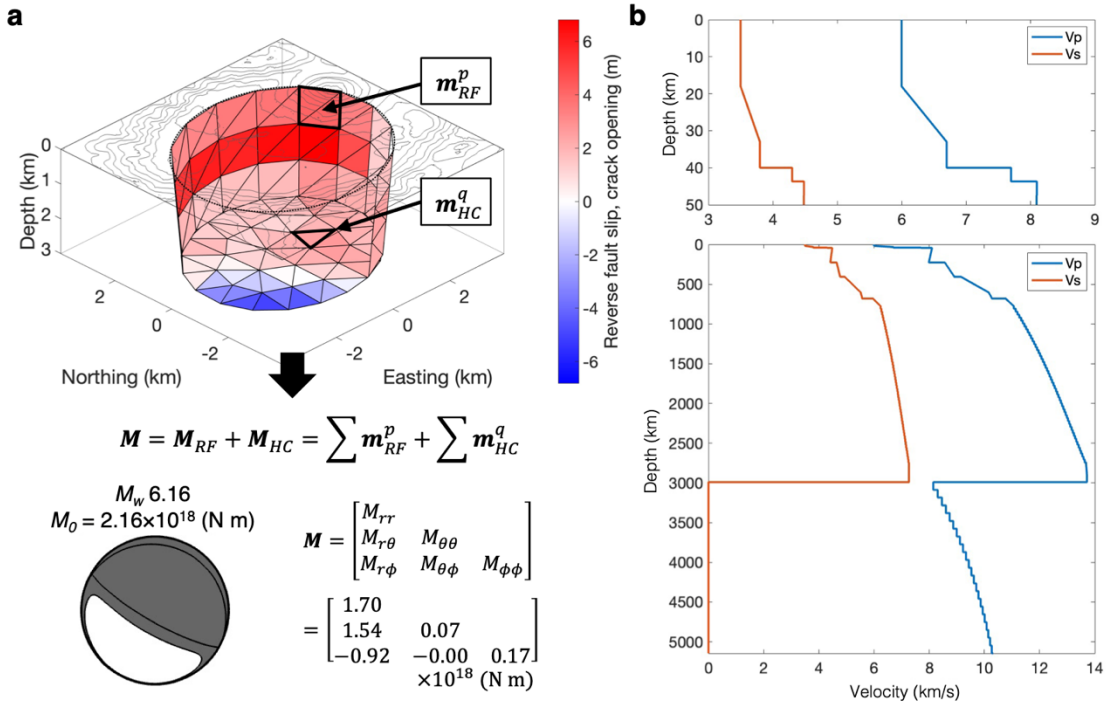

Figure S6. Moment tensor computation and 1-D velocity structure. (**a**) Moment tensor computation process. As an example, the case of the best-fit source model is shown (Figure 4a). (**b**) 1-D velocity structure used in this study (bottom panel). In the top panel, the velocities down to a depth of 50 km are shown.

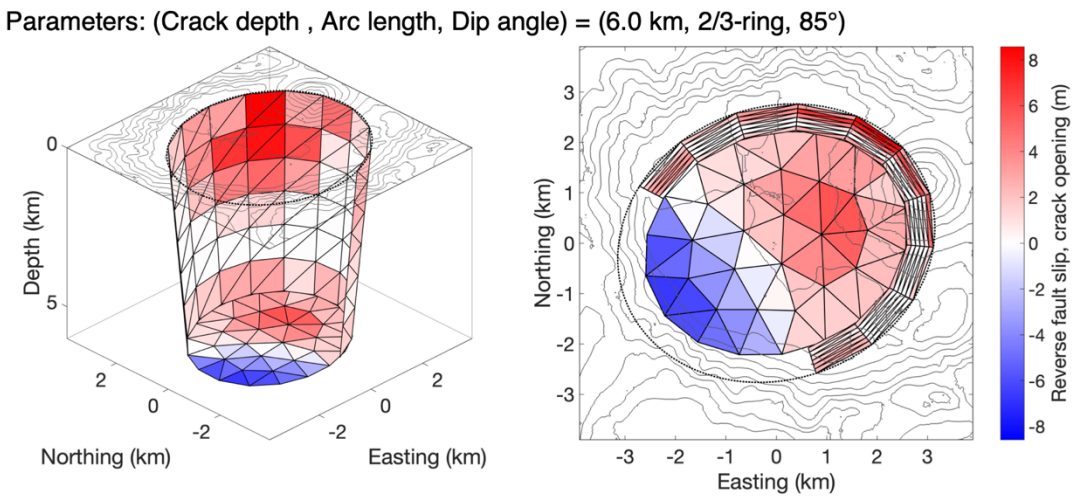

Figure S7. Source model inverted from the tsunami waveform inversion, in which we assume a horizontal crack at a depth of 6 km. Color coding is the same as for Figure 4a. We consider this model to be unrealistic (see the text for explanation in Section 5).

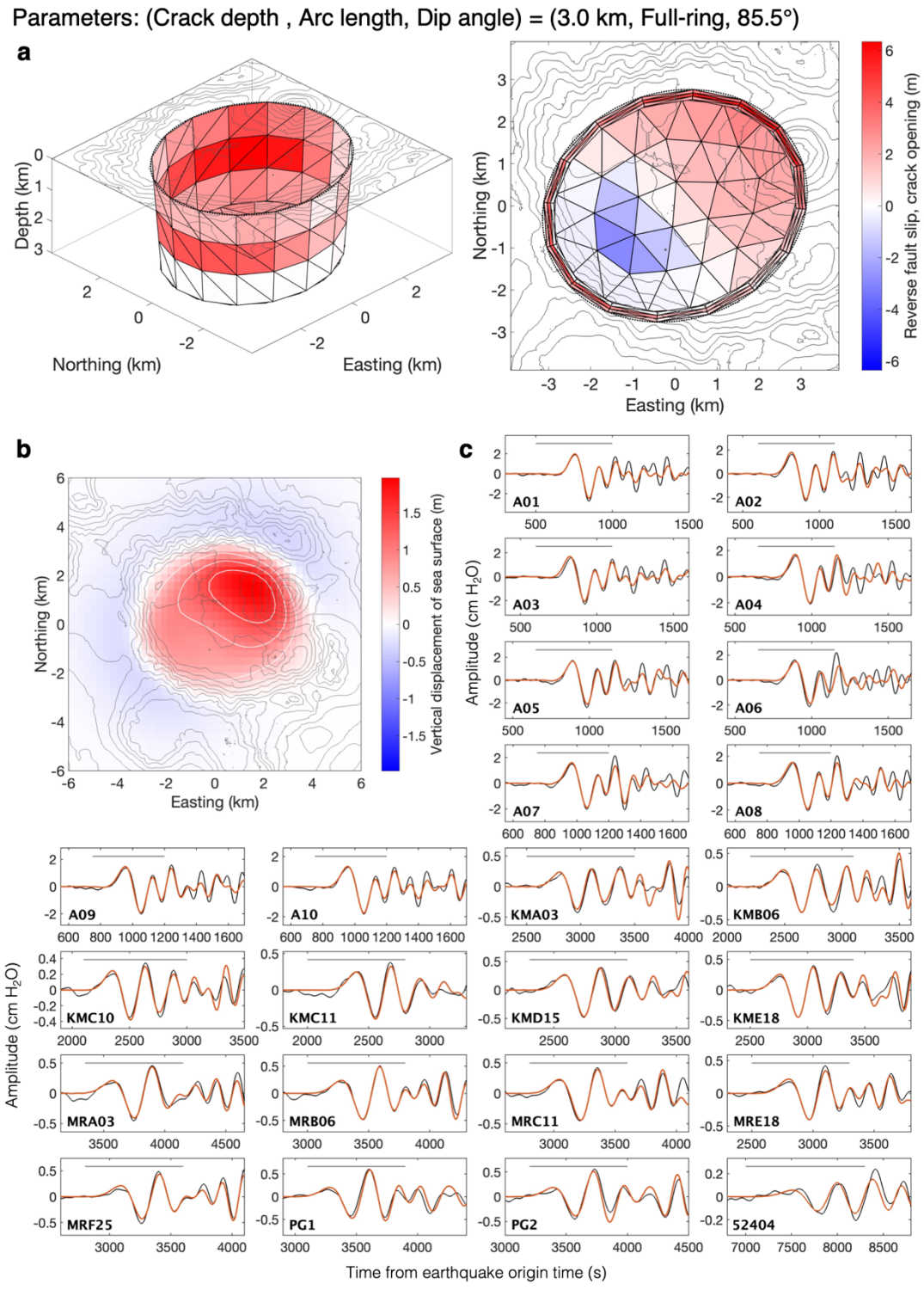

Figure S8. Source modeling results when we assume the source parameters: (Crack depth, Arc length, Dip angle) = (3.0 km, full-ring, 85.5°). (**a**) Source model. See the caption of Figure 4a. (**b**) Vertical displacement of sea surface and (**c**) the tsunami waveforms expected from the model. See the captions of Figure 6.

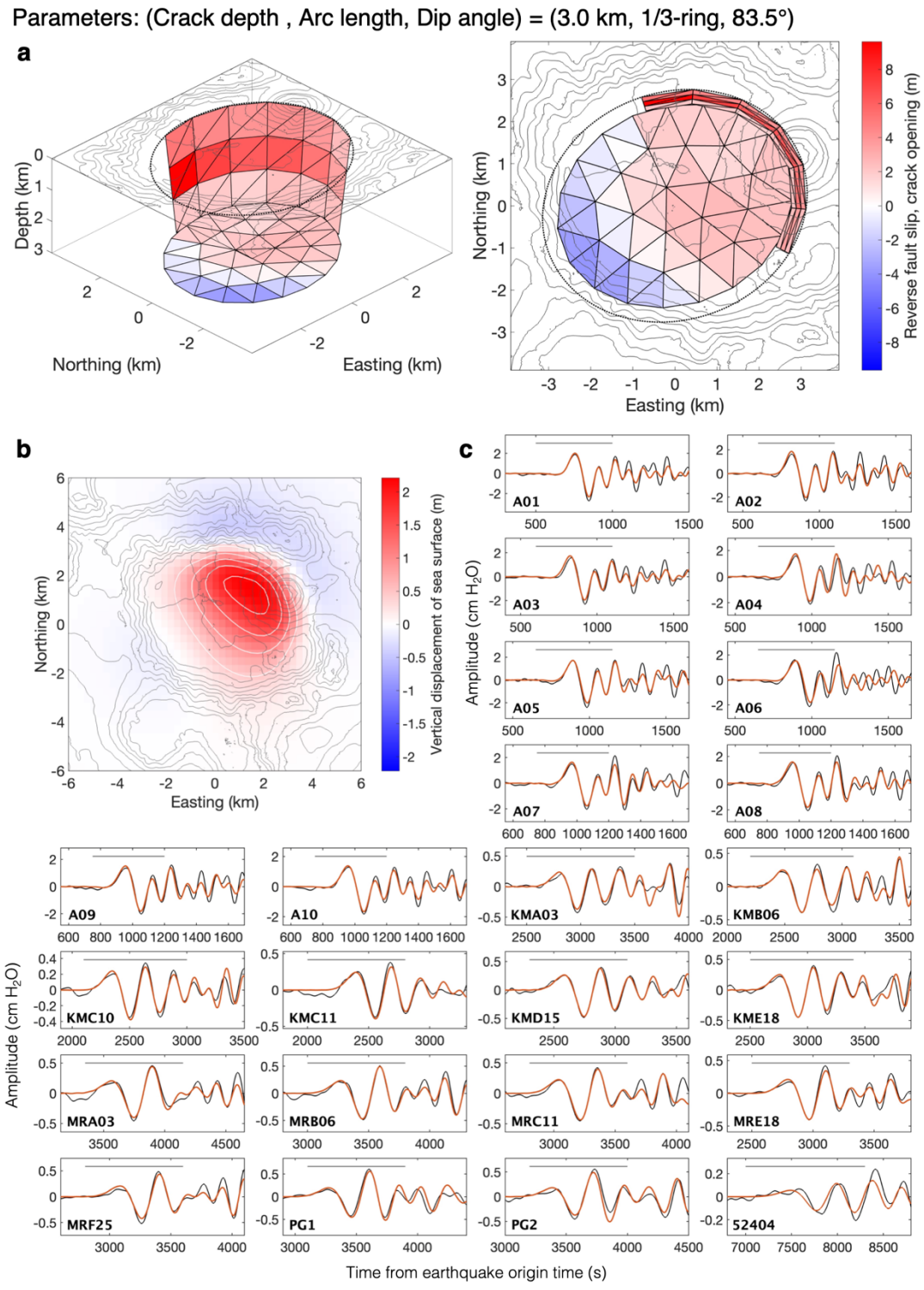

Figure S9. Same as Figure S8, but for those when we assume the source parameters: (Crack depth, Arc length, Dip angle) = (3.0 km, 1/3-ring, 83.5°).

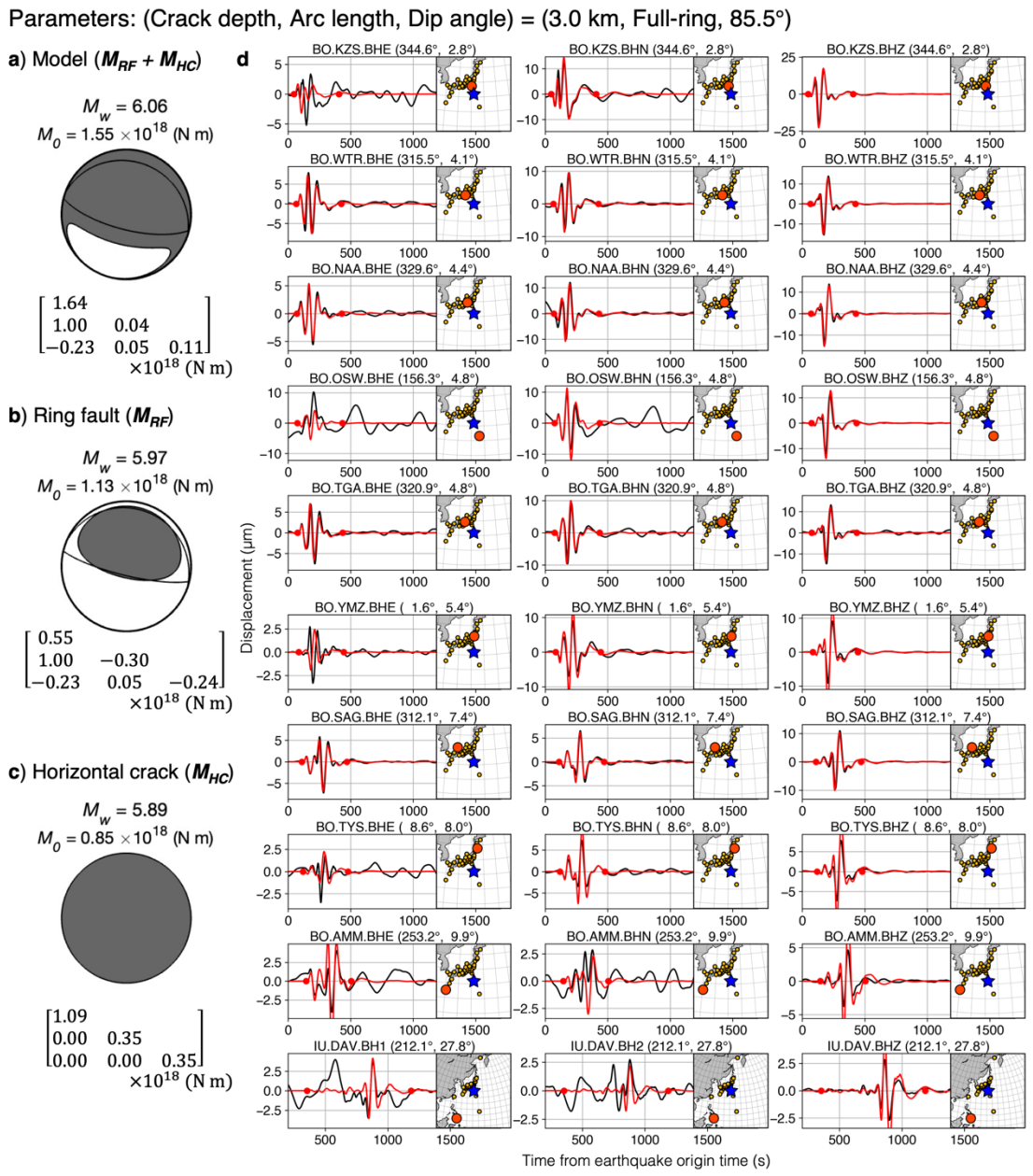

Figure S10. Same as Figure 8, but for the full-ring model shown in Figure S8.

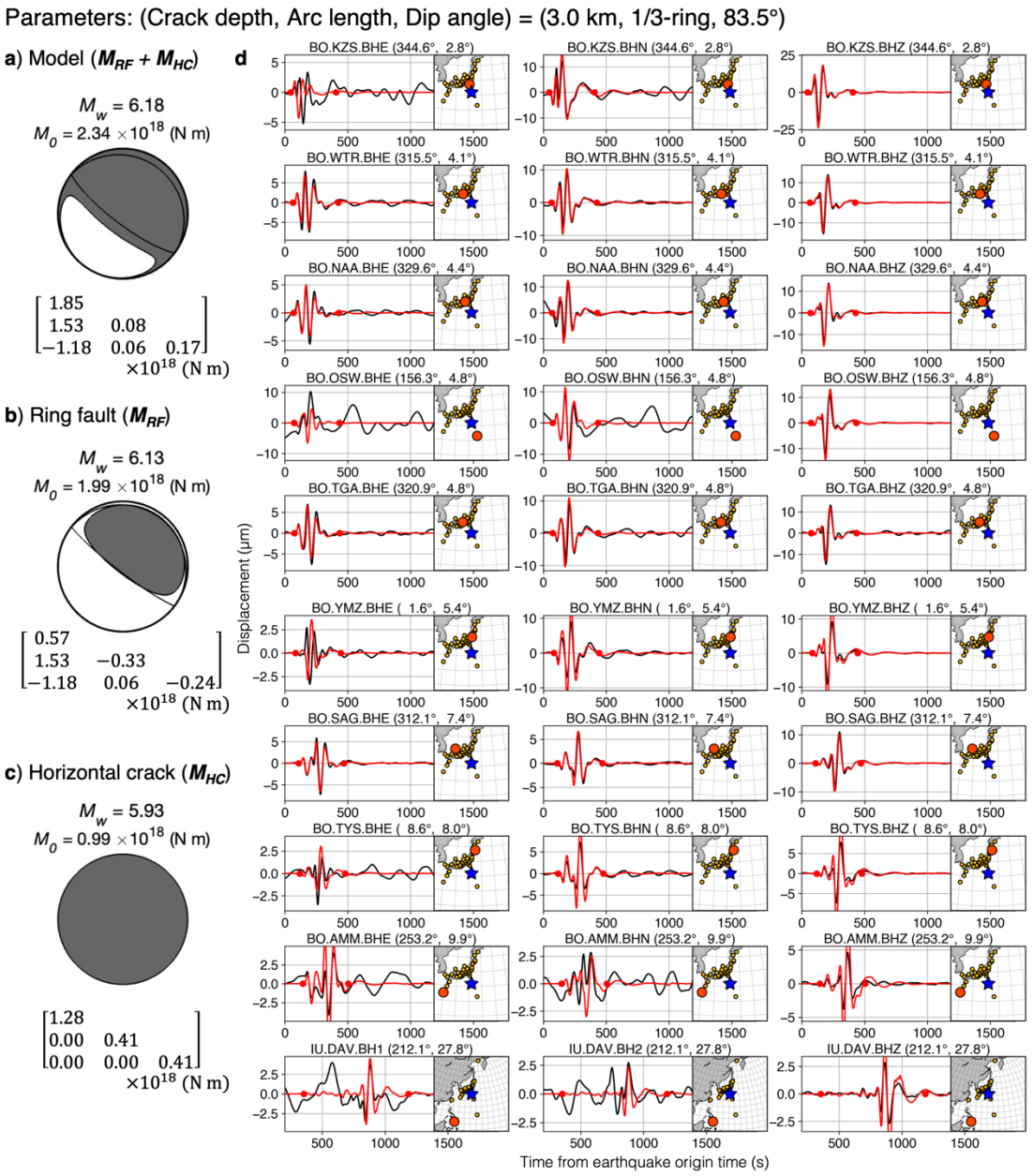

Figure S11. Same as Figure 8, but for the 1/3-ring model shown in Figure S9.

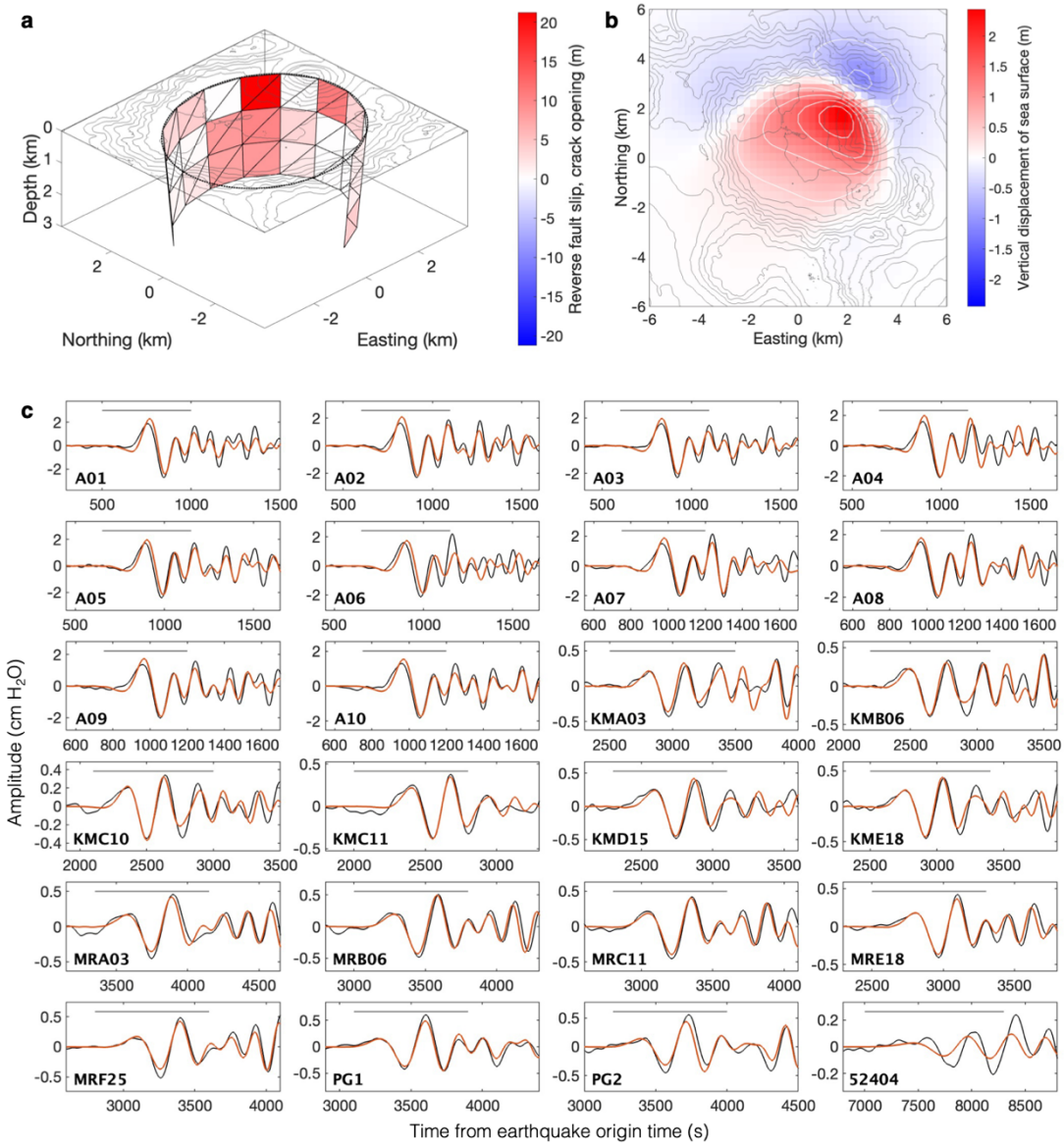

Figure S12. Source model inverted from the tsunami waveform inversion, in which we assume only the ring fault. See the caption of Figures 4a and 6. Note that with only the ring fault, the waveform fit is overall worse, compared to the tsunami waveforms from the fault-crack composite source model (Figure 6).

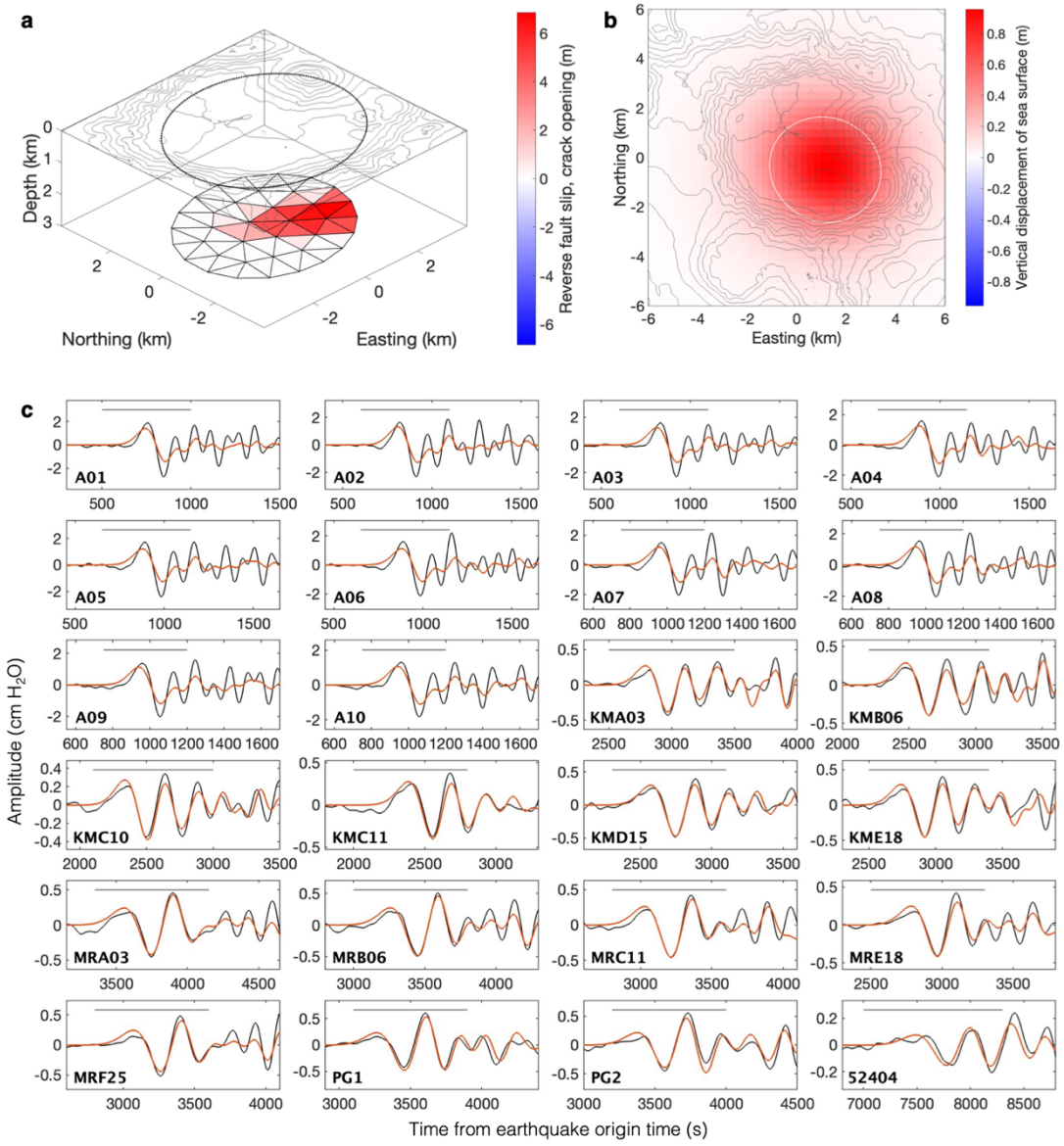

Figure S13. Source model inverted from the tsunami waveform inversion, in which we assume only the horizontal crack. See the caption of Figures 4a and 6. Note that with only the horizontal crack, the waveform fit is clearly worse, compared to the tsunami waveforms from the fault-crack composite source model (Figure 6).

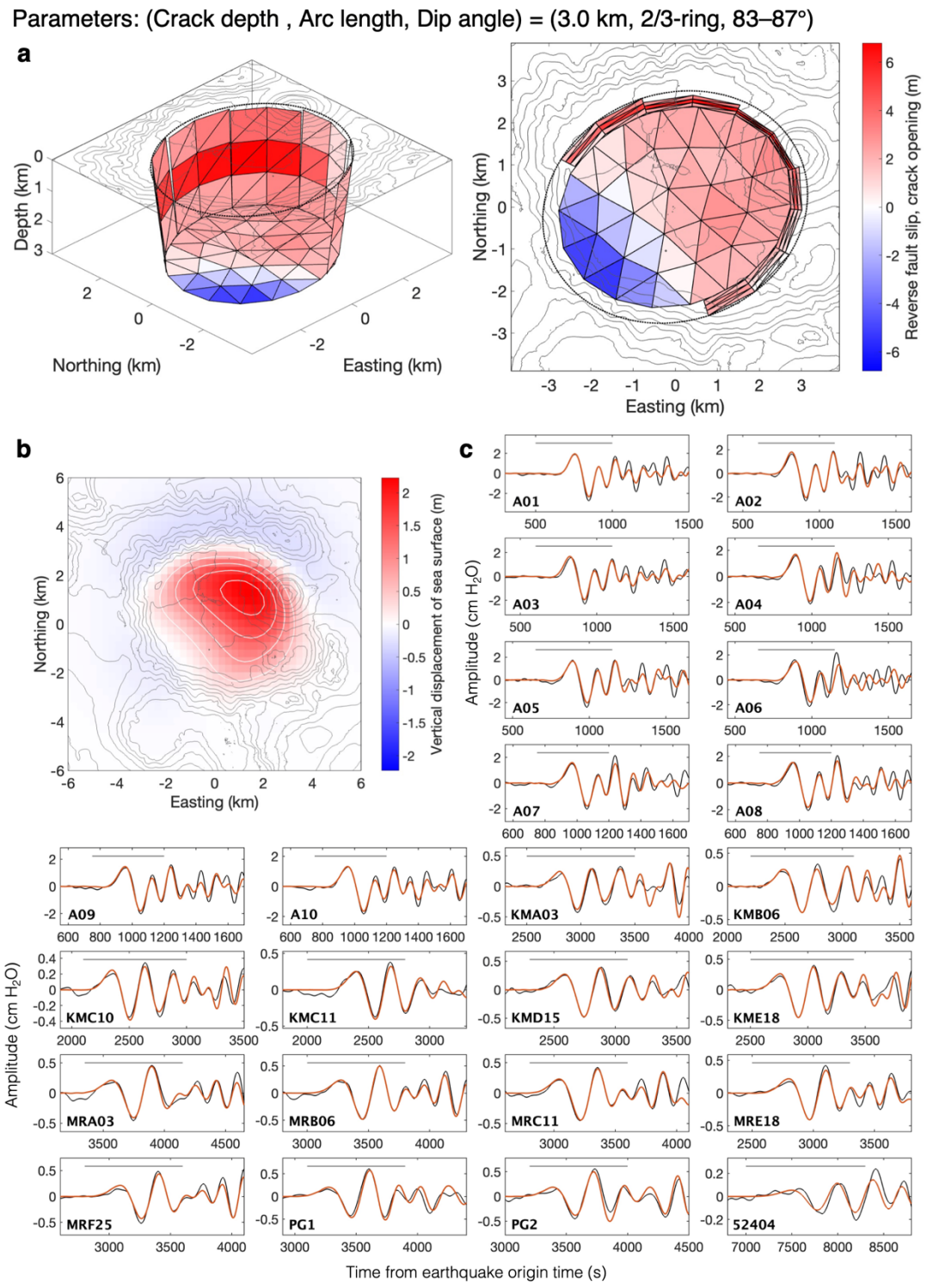

Figure S14. Same as Figure S8, but for those when we assume the source parameters: (Crack depth, Arc length, Dip angle) = (3.0 km, 2/3-ring, 83–87°). Note that the dip angle is not uniform along the ring fault (see Text S3).

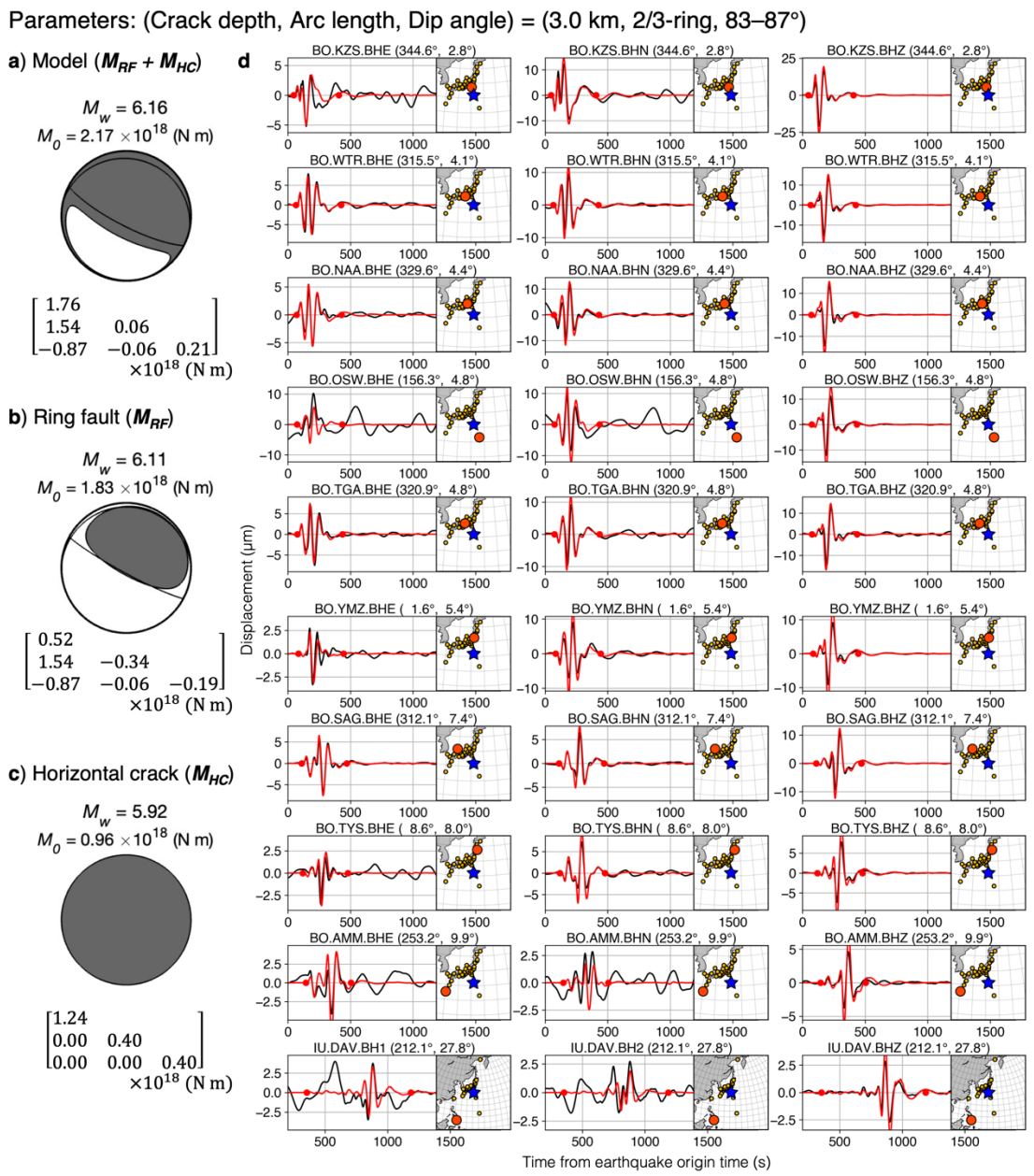

Figure S15. Same as Figure 8, but for the 1/3-ring model shown in Figure S14.

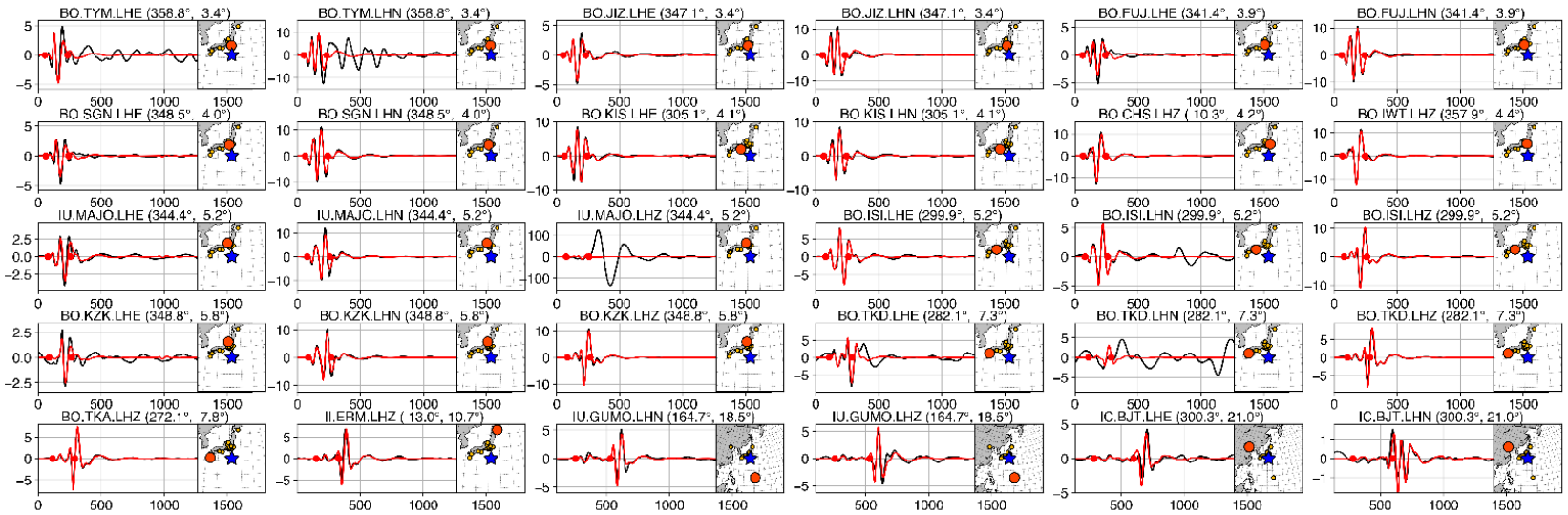

Figure S16. Model performance of the MT inversion for the 1996 earthquake. The vertical and horizontal axes represent displacement (in the [μm] scale) and time from the earthquake origin time (in the [s] scale). Red and black lines represent synthetic and observed waveforms, respectively. The time window for the inversion is indicated by red dots.

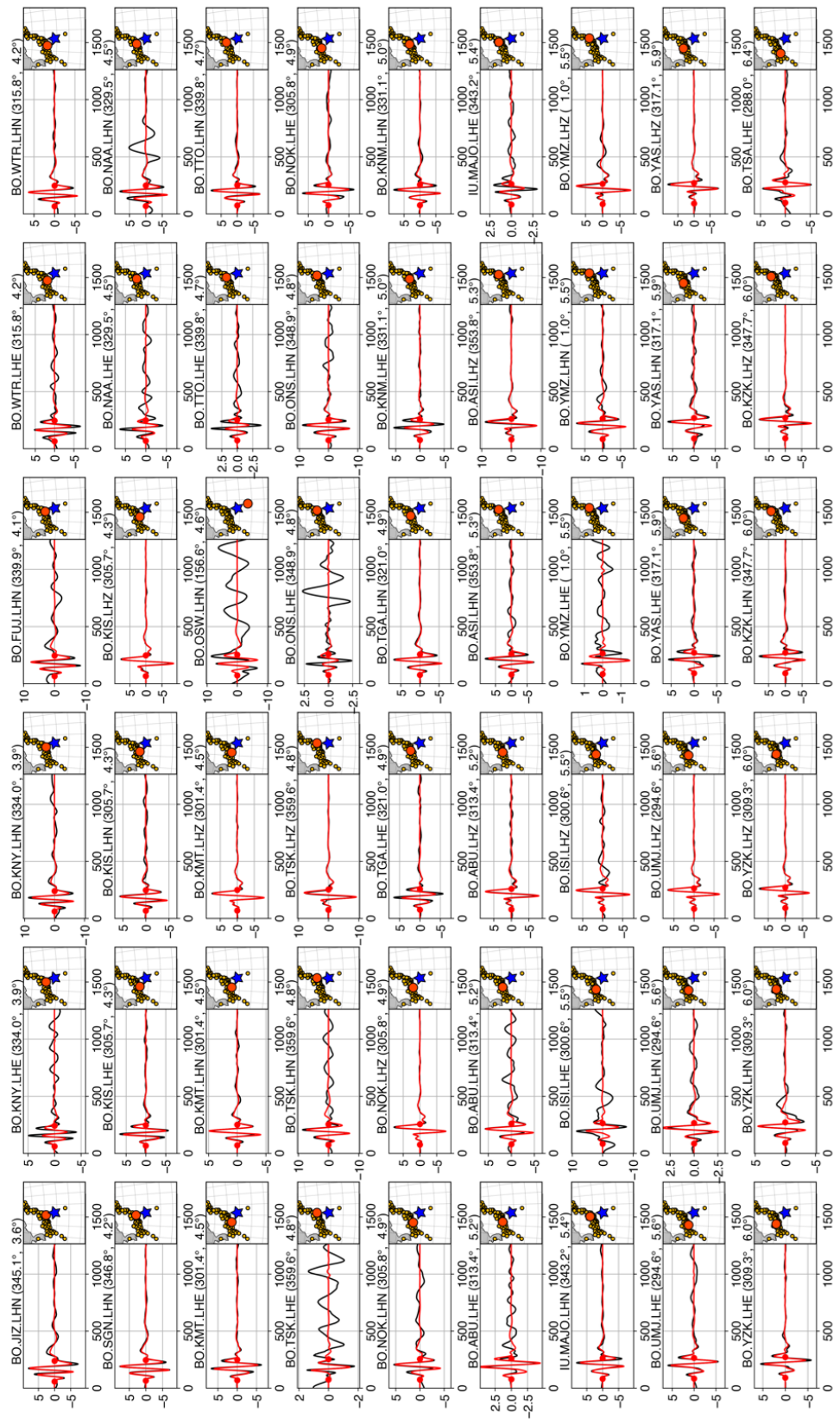

Figure S17. Model performance of the MT inversion for the 2006 earthquake.

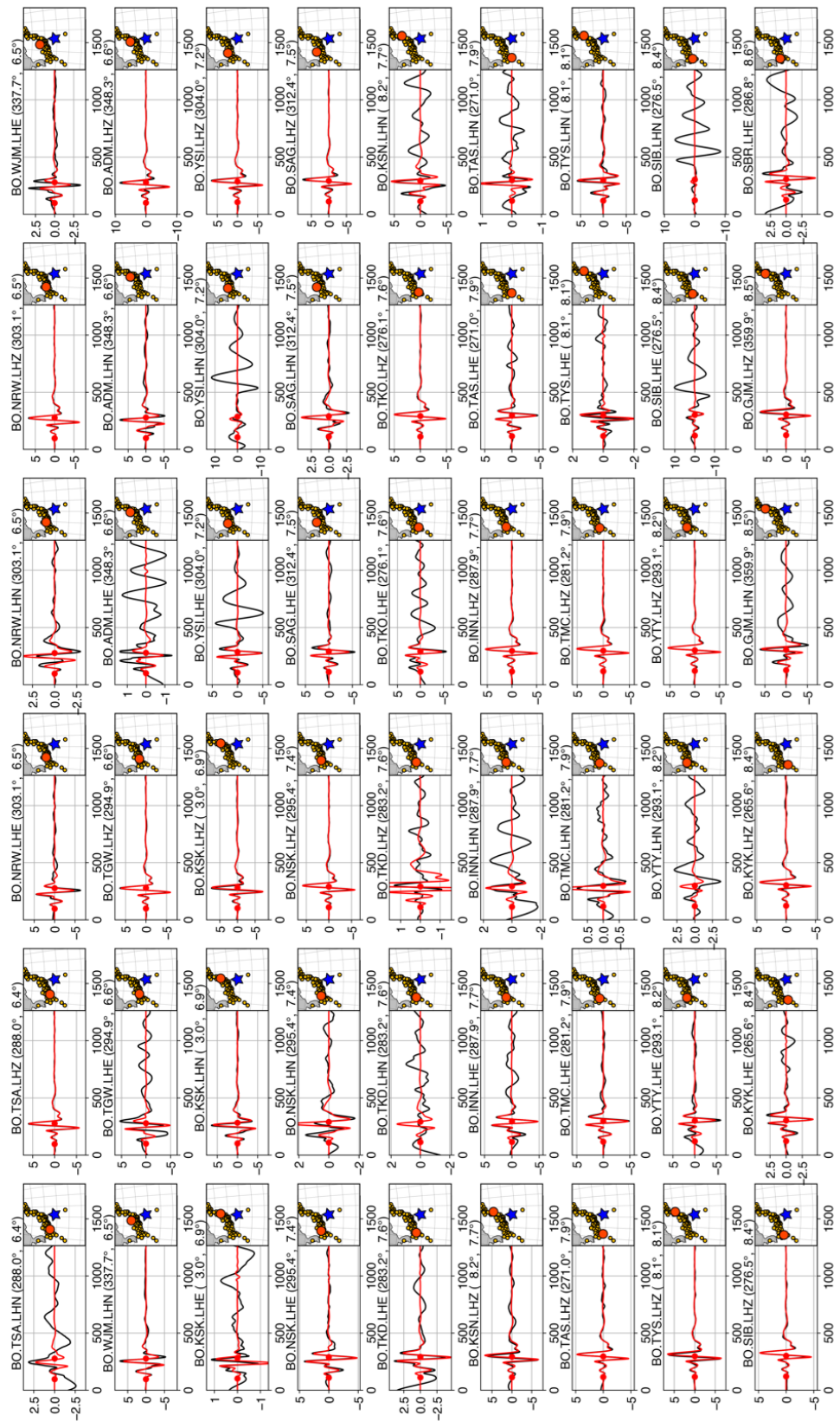

Figure S17. Model performance of the MT inversion for the 2006 earthquake (continued).

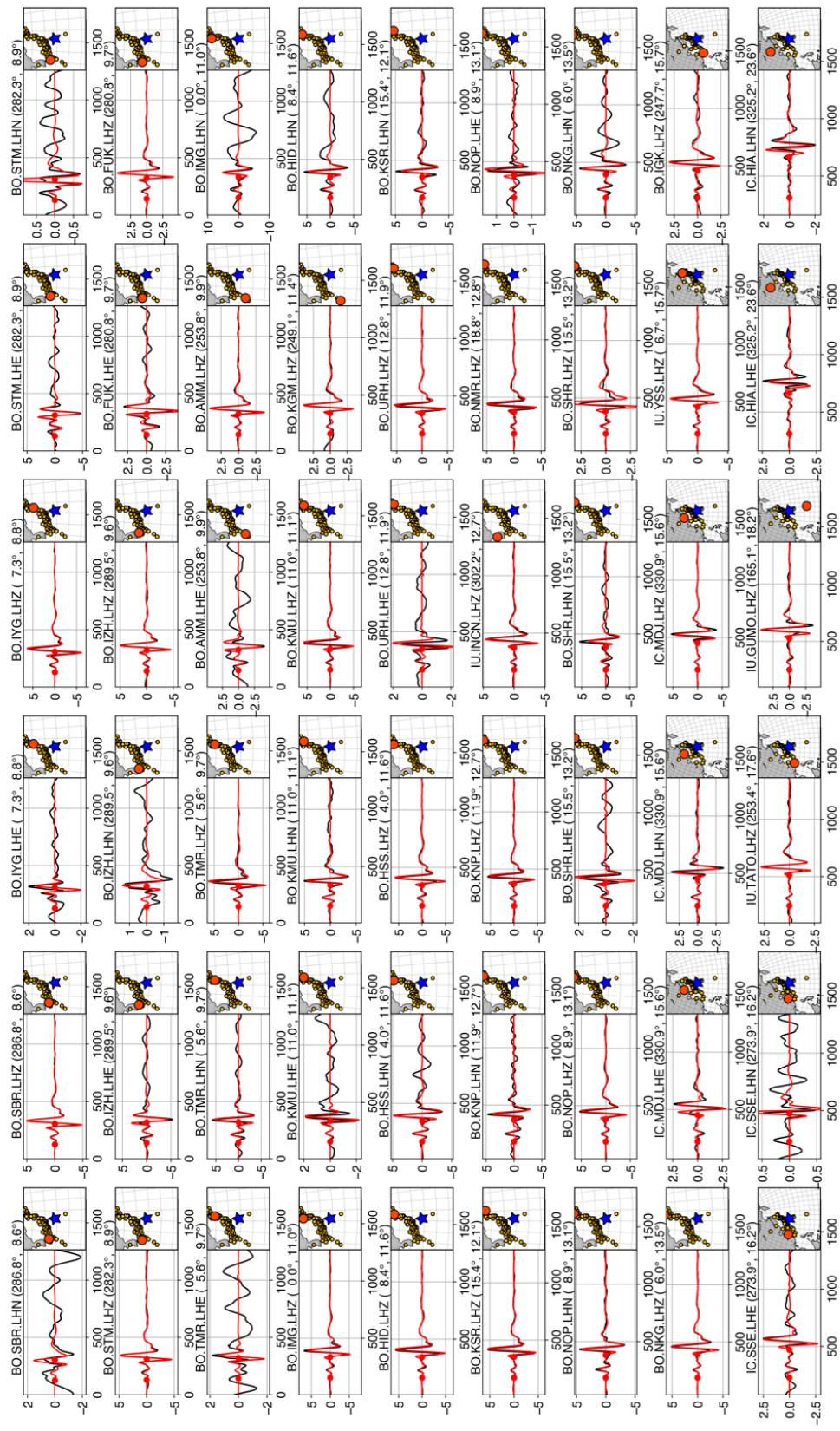

Figure S17. Model performance of the MT inversion for the 2006 earthquake (continued).

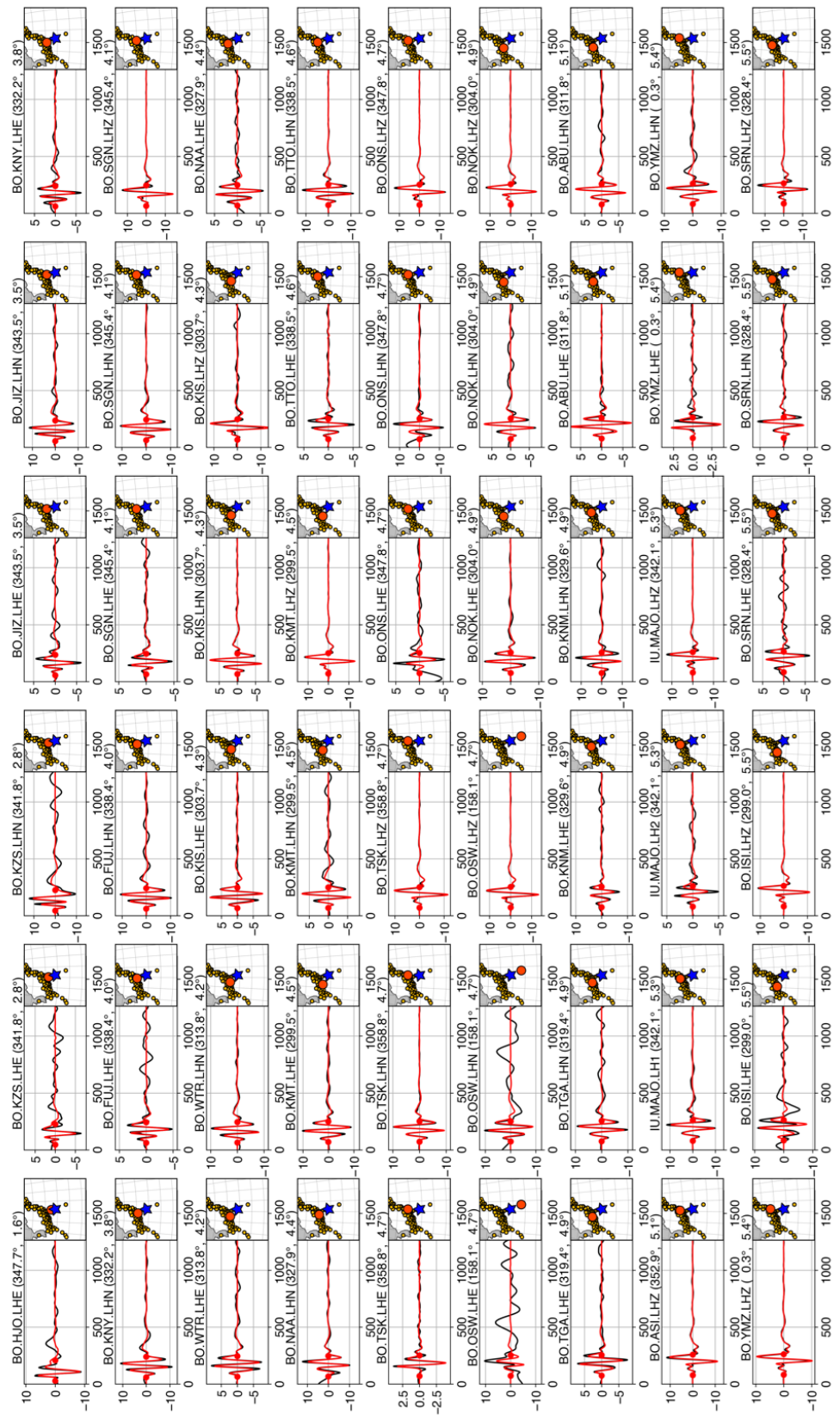

Figure S18. Model performance of the MT inversion for the 2015 earthquake.

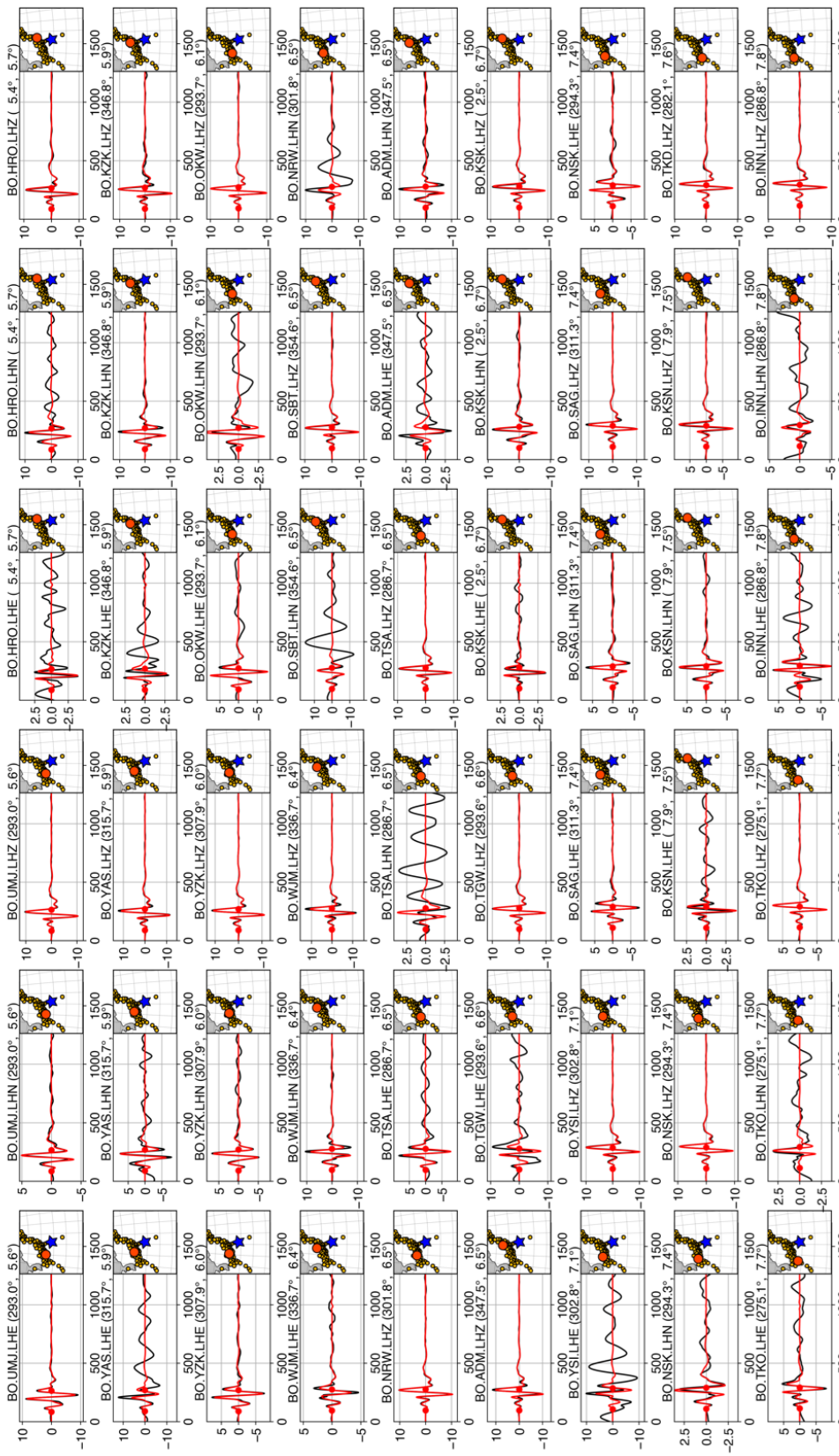

Figure S18. Model performance of the MT inversion for the 2015 earthquake (continued).

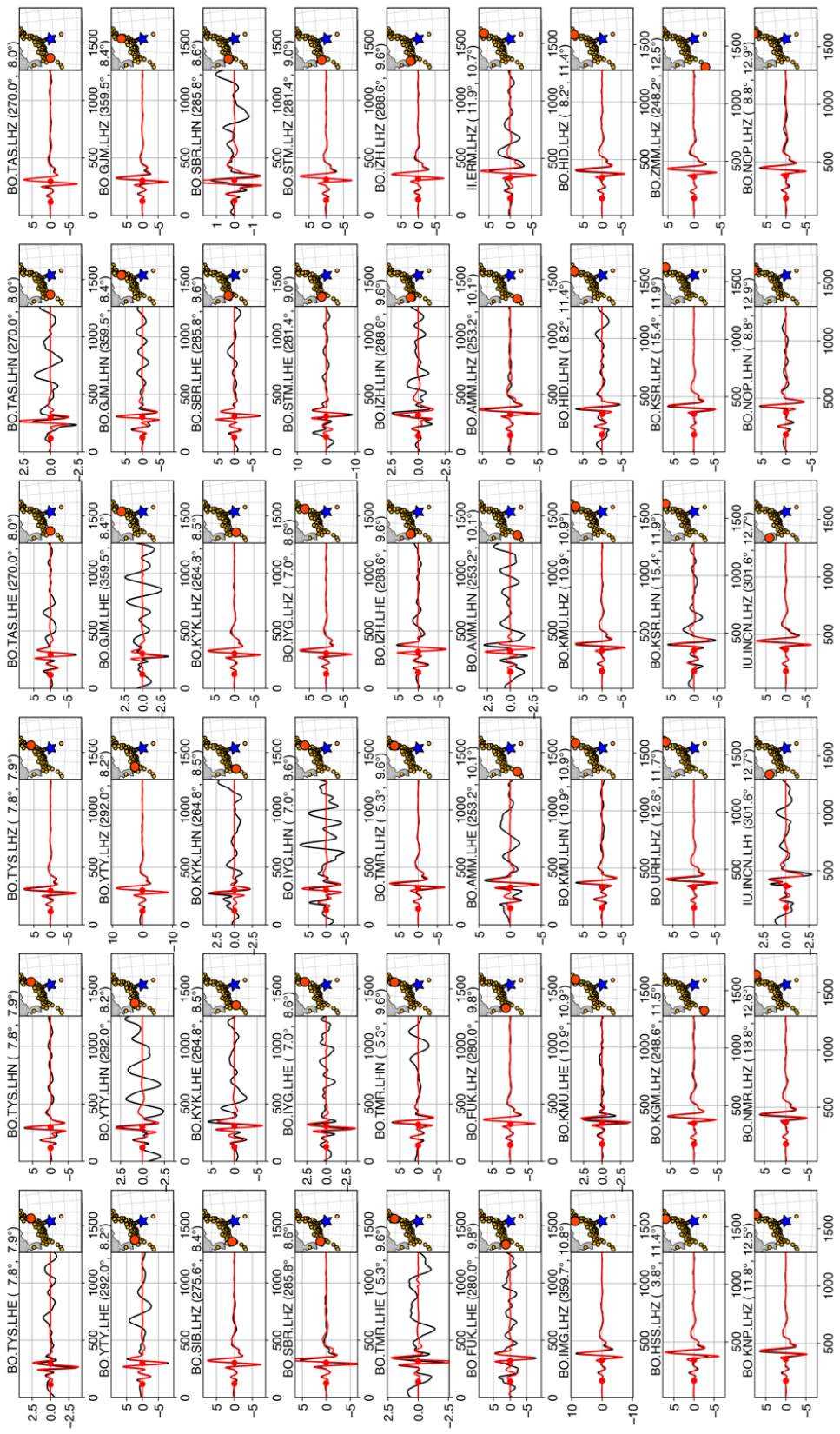

Figure S18. Model performance of the MT inversion for the 2015 earthquake (continued).

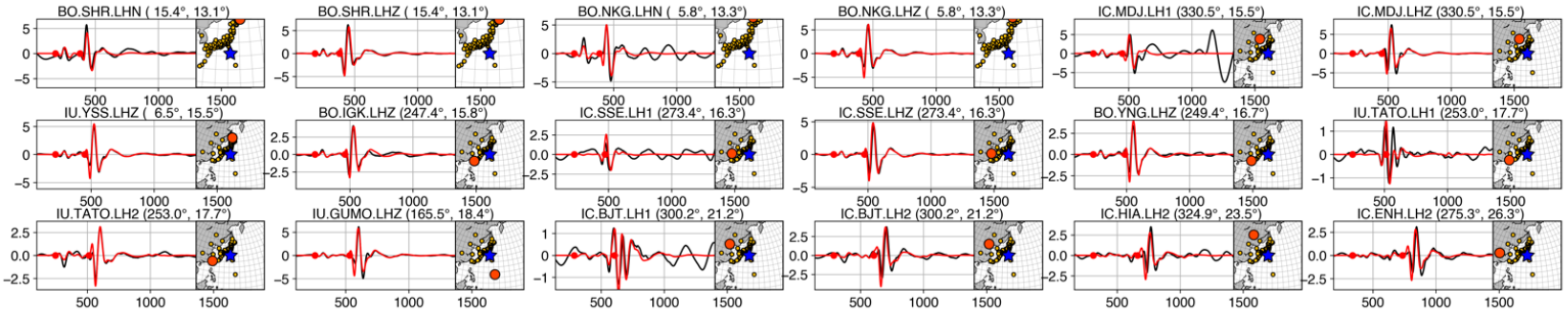

Figure S18 Model performance of the MT inversion for the 2015 earthquake (continued).

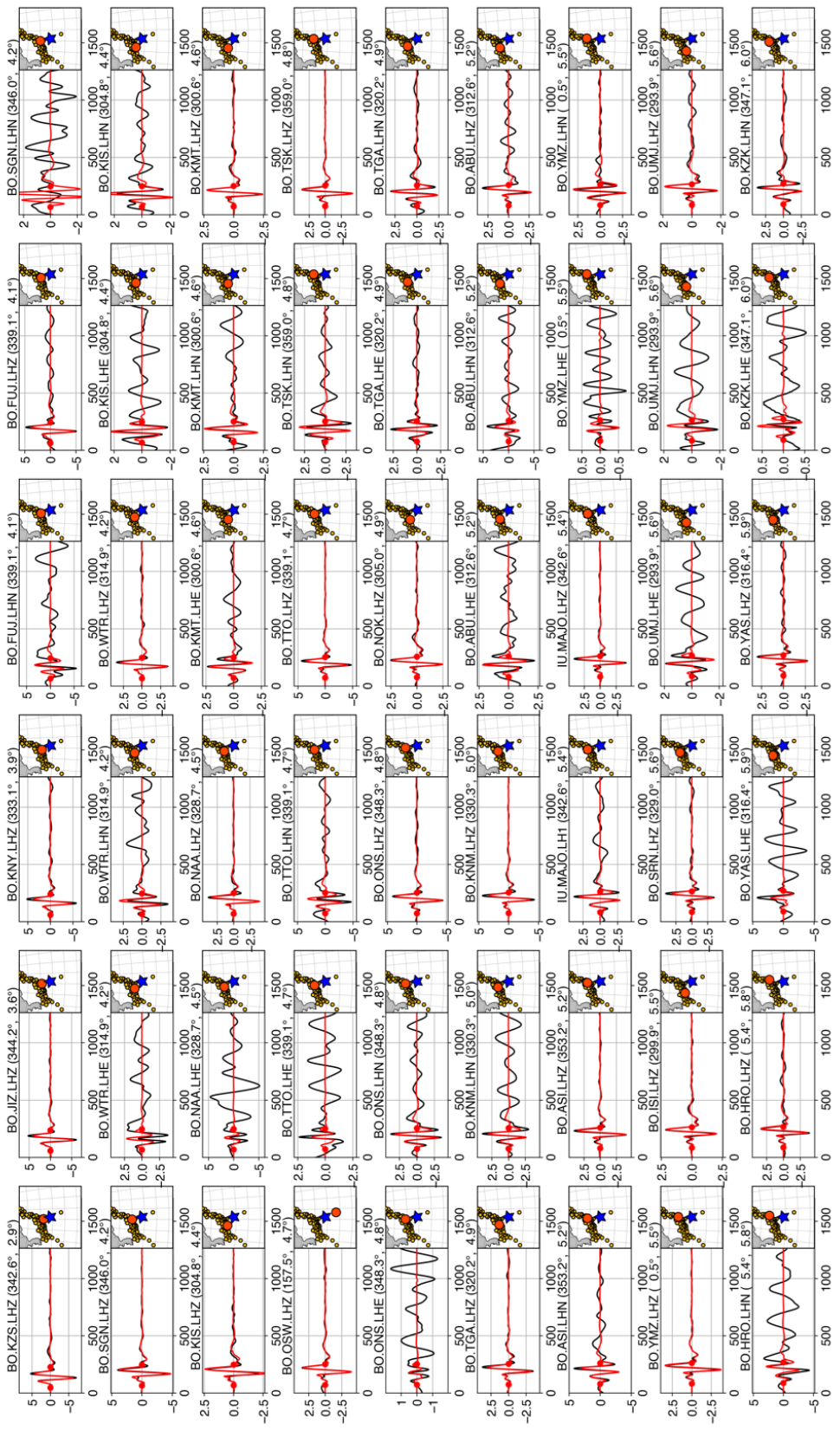

Figure S19. Model performance of the MT inversion for the 2018 earthquake.

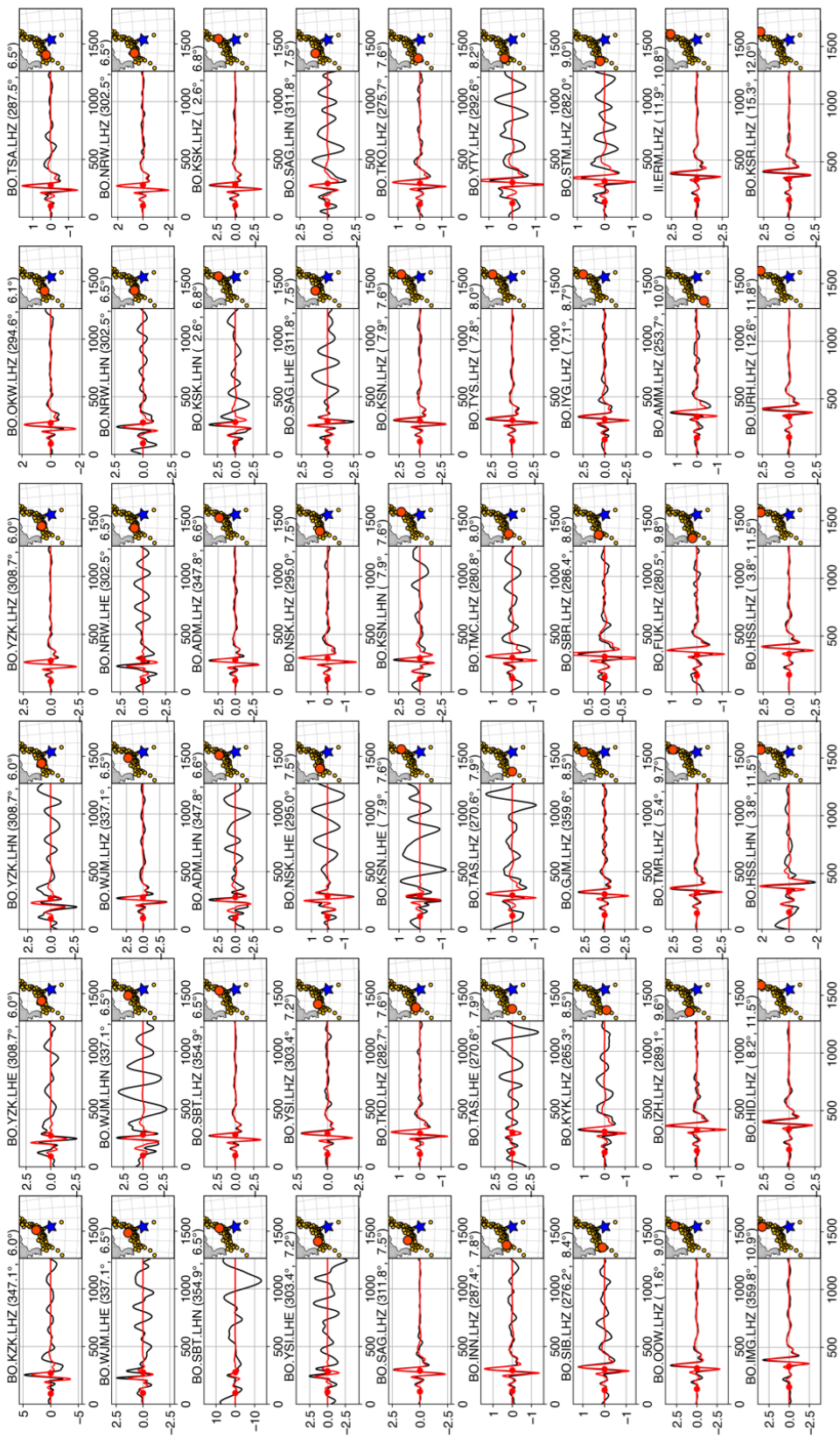

Figure S19. Model performance of the MT inversion for the 2018 earthquake (continued).

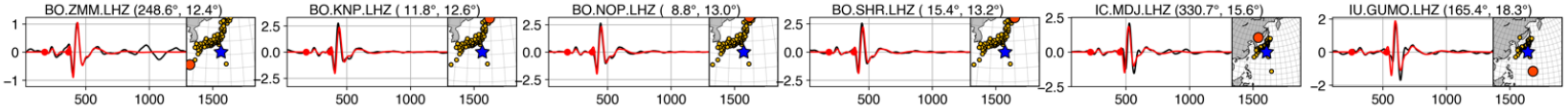

Figure S19. Model performance of the MT inversion for the 2018 earthquake (continued).

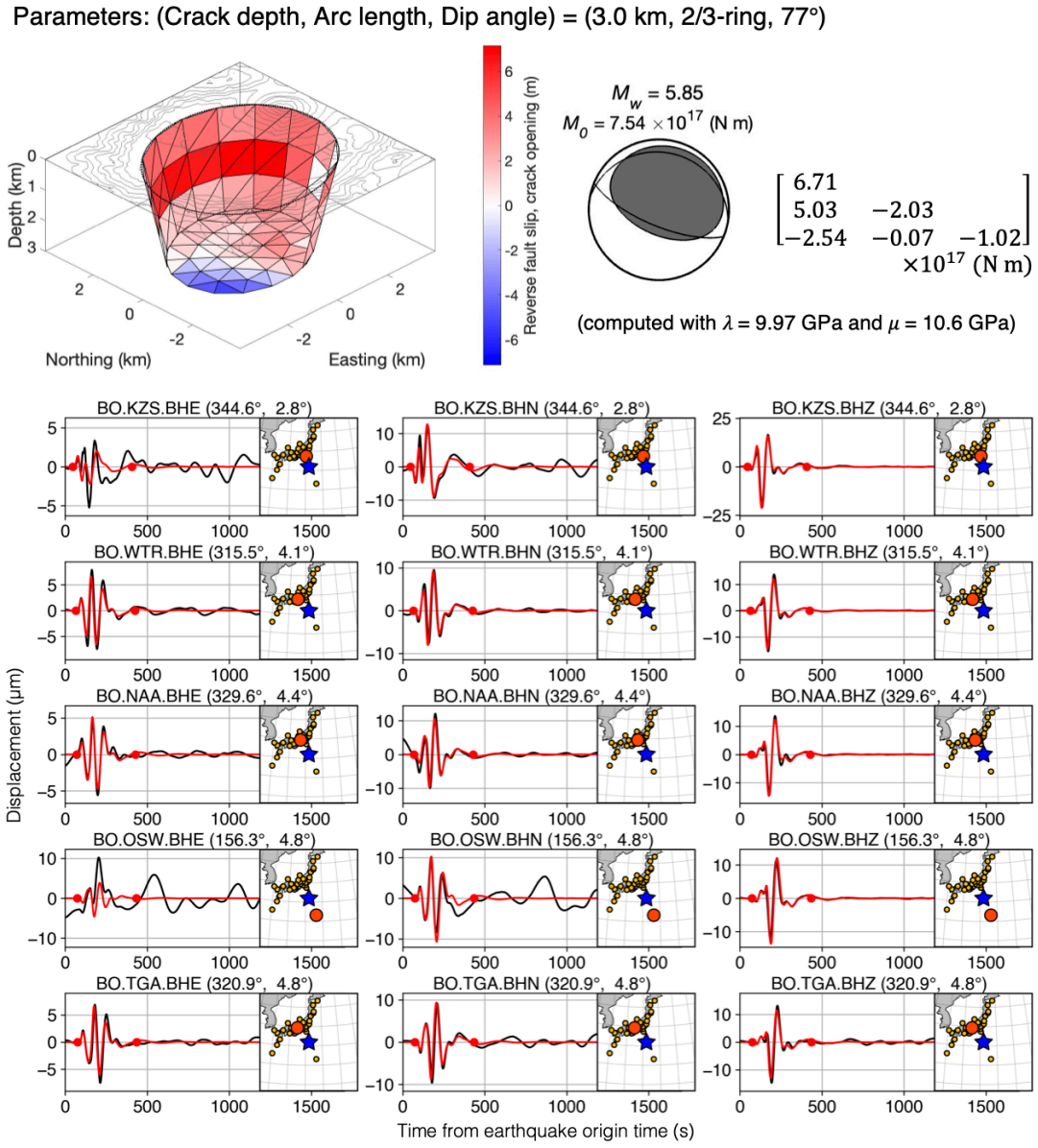

Figure S20. Synthetic long-period seismic waveforms when we assume low rigidity ($\boldsymbol{\lambda}$ = 9.97 GPa and $\boldsymbol{\mu}$ = 10.6 GPa) for the moment tensor computation. This shows the model with the 2/3-ring fault with a dip angle of 77°.

Event	Date (Y/M/D)	Time (h:m:s)	Longitude	Latitudes	Depth (km)	M_W	M_S
1	1984/6/13	2:29:29	139.93°	31.39°	15.2	5.6	5.4
2	1996/9/4	18:16:07	140.06°	31.48°	24.4	5.7	5.1
3	2006/1/1	7:12:07	140.07°	31.51°	12	5.6	5.0
4	2015/5/2	16:50:50	139.94°	31.47°	12	5.7	5.7
5	2018/5/6	6:04:06	139.98°	31.51°	12	5.4	5.4

Table S1. Earthquake information of volcanic earthquakes at Sumisu caldera, reported by the GCMT catalog (Ekström, Nettles, and Dziewoński 2012). Note that shallow source depths cannot be determined accurately with long-period seismic data used for the catalogue.

Network	Station code	Distance (degree)	Azimuth (degree)
F-net	KZS	2.82	344.57
F-net	JIZ	3.54	345.74
F-net	KNY	3.77	334.25
F-net	WTR	4.11	315.49
F-net	SGN	4.12	347.31
F-net	KIS	4.24	305.17
F-net	NAA	4.36	329.6
F-net	KMT	4.43	300.79
F-net	TTO	4.63	340.16
F-net	TSK	4.72	0.36
F-net	OSW	4.75	156.29
F-net	NOK	4.78	305.26
F-net	TGA	4.82	320.88
F-net	KNM	4.85	331.16
GSN	MAJO	5.28	343.59
F-net	YMZ	5.43	1.62
F-net	UMJ	5.49	293.93
F-net	SRN	5.5	329.74
F-net	YZK	5.9	309
F-net	WJM	6.41	337.87
F-net	KSK	6.77	3.54
F-net	NSK	7.34	294.95
F-net	SAG	7.36	312.11
F-net	TKO	7.53	275.4
F-net	KSN	7.57	8.77
F-net	TYS	7.97	8.64
F-net	KYK	8.36	264.9
F-net	SBR	8.52	286.26
F-net	IZH	9.5	289.03
F-net	TMR	9.66	6
F-net	AMM	9.91	253.18
F-net	KMU	10.98	11.41
GSN	TATO	17.58	252.97
GSN	GUMO	18.35	164.98
GSN	DAV	27.8	212.13
GSN	MA2	29	11.26

Table S2. Stations used for the computation of the long-period seismic waves. Station list of broad-band seismic stations used for the forward simulation of long-period seismic waves. For each station, we use the record of the three components.

Event	M_w	M_0 (x 10^{18} N m)	Moment tensor (x 10^{18} N m)						Half duration (s)
			M_{rr}	$M_{\theta\theta}$	$M_{\phi\phi}$	$M_{r\theta}$	$M_{r\phi}$	$M_{\theta\phi}$	
1996	5.99	1.20	0.384	-0.221	-0.164	0.282	-1.140	-0.069	5.3
2006	5.88	0.82	0.286	-0.189	-0.097	-0.159	-0.780	-0.024	8.0
2015	6.01	1.30	0.385	-0.225	-0.160	-0.311	-1.226	-0.071	5.0
2018	5.58	0.28	0.103	-0.091	-0.011	-0.107	-0.252	-0.006	4.0

Table S3. Results of the moment tensor analysis. Moment magnitudes, scalar seismic moments, moment tensors, and half durations of the repeating earthquakes. Note that $\boldsymbol{M_{r\theta}}$ and $\boldsymbol{M_{r\phi}}$ determined from long-period seismic waveforms are unreliable due to shallow source depths (Sandanbata et al. 2021).

Data Set S1. Fault-crack composite source models (separate file). This dataset includes four models presented in Figures 4a, S8a, S9a, and S14a.

Supplementary References

Duputel, Z., Rivera, L., Kanamori, H., & Hayes, G. (2012). W phase source inversion for moderate to large earthquakes (1990–2010). *Geophysical Journal International*, *189*(2), 1125–1147. https://doi.org/10.1111/j.1365-246X.2012.05419.x.

Ekström, G., Nettles, M., & Dziewoński, A. M. (2012). The global CMT project 2004–2010: Centroid-moment tensors for 13,017 earthquakes. *Physics of the Earth and Planetary Interiors*, *200-201*, 1–9. https://doi.org/10.1016/j.pepi.2012.04.002.

Hayes, G. P., Rivera, L., & Kanamori, H. (2009). Source Inversion of the W-Phase: Real-time Implementation and Extension to Low Magnitudes. *Seismological Research Letters*, *80*(5), 817–822. https://doi.org/10.1785/gssrl.80.5.817.

Kanamori, H., & Rivera, L. (2008). Source inversion of Wphase: speeding up seismic tsunami warning. *Geophysical Journal International*, *175*(1), 222–238. https://doi.org/10.1111/j.1365-246X.2008.03887.x.

Kodaira, S., Sato, T., Takahashi, N., Ito, A., Tamura, Y., Tatsumi, Y., & Kaneda, Y. (2007). Seismological evidence for variable growth of crust along the Izu intraoceanic arc. *Journal of Geophysical Research*, *112*(B5). https://doi.org/10.1029/2006jb004593.

Sandanbata, O., Kanamori, H., Rivera, L., Zhan, Z., Watada, S., & Satake, K. (2021). Moment tensors of ring-faulting at active volcanoes: Insights into vertical-CLVD earthquakes at the Sierra Negra caldera, Galápagos islands. *Journal of Geophysical Research, [Solid Earth]*, *126*(6), e2021JB021693. https://doi.org/10.1029/2021jb021693.